Development of interferometric techniques for nuclei size measurement in cavitation tunnel

Loï c M ées, Denis Lebrun, Daniel Allano, Françoise Walle, Yves Lecoffre, Romuald Boucheron, Didier Fréchou

28th Symposium on Naval Hydrodynamics
Pasadena, California, 12-17 September 2010

Development of interferometric techniques for nuclei size measurement in cavitation tunnel

Loic Mées[1], Denis Lebrun[2], Daniel Allano[2], Françoise Walle[2],
Yves Lecoffre[3], Romuald Boucheron[4], Didier Fréchou[4],

[1]CNRS-LMFA Ecole Centrale de Lyon, France, loic.mees@ec-lyon.fr,
[2]CORIA Université de Rouen, France, lebrun@coria.fr,
[3]YLec Consultants, 24 Bvd de la Chantourne 38700 La Tronche France, ylec@wanadoo.fr,
[4]DGA Techniques Hydrodynamiques, Val de reuil France, corresponding author,
dider.frechou@dga.defense.gouv.fr

ABSTRACT

The knowledge of the nuclei content is essential in naval hydrodynamics for cavitation inception prediction on propellers and hydrofoils. As a matter of fact, tip vortex cavitation which is, generally, the first cavitation to occur on foils or propellers, is very sensitive to the nuclei content. Typically, the nuclei we are looking at, are tiny bubbles which sizes range from 1µm up to 100µm.

Two different types of techniques are generally used: optical techniques that measure the nuclei size and Venturi techniques which measure the critical pressure of the nuclei.

We present here developments of two new optical techniques: the digital in-line holography technique and the Interferometric Laser Imaging Technique based on the PIV optical arrangement. Both techniques have been implemented in the French Large Cavitation Tunnel so called GTH and comparative measurements have been done with CSM technique.

INTRODUCTION

The operational requirements for naval and research vessels has seen an increasing demand for quieter ships. Hence, the management of a ship's hydrodynamic signature requires better and more reliable estimates of propeller noise. One of the major sources of radiated noise is the occurrence of cavitation on the ship propeller. This makes the cavitation inception prediction a critical issue to assess for propeller model scale testing in hydrodynamic tunnel.

The water quality or nuclei content control is required in a hydrodynamic tunnel dedicated to cavitation studies [Cavitation Committee Report of 20th ITTC, 1993]. Several studies, for instance [Gindroz & Billet 1993, Billet & al 1996], have confirmed the merit of the nuclei control for cavitation tests. Most of the cavitation tunnels are controlling the nuclei content indirectly by controlling the dissolved air content of the water. The French large cavitation tunnel is a rather unique facility in which the nuclei content is controlled through microbubbles injection generator [Lecoffre & al 1987; Fréchou & al, 2000] independently of the dissolved air content control. The water quality produced in standard tunnels always varies with time and tests sequences. The French large cavitation tunnel is one of the rare facilities in which the nuclei content is controlled through microbubbles injection [Lecoffre & al 1987; Fréchou & al, 2000] independently of the dissolved air content control. Other tunnels like AMC in Australia, LEGI in Grenoble France and pump or turbine loops use the same technique. This method guarantees the repeatability of the test conditions over time. The nuclei content measurement is required to ensure that the critical pressure of the water is close to the vapor pressure and to know the density of active nuclei. This implies to seed the flow with bubbles sizes of about 20µm - 100µm.

It is practically necessary to have the nuclei content high enough to detect easily cavitation inception events. At model scale on propeller, cavitation inception is generally detected from visual observations either directly through test

section or on recorded video images. It is a common rule to say that the cavitation inception operating conditions correspond to a cavitation event rate in the order of one per second. The cavitation event rate is directly related to the nuclei concentration:

$$\xi(nber/s) = N(nber/m^3)\cdot S(m^2)\cdot V(m/s)) \quad \text{eq.(4)}$$

ξ : number of cavitating nuclei per time unit
N : number of cavitating nuclei per volume unit
S : cross-section area in which the nuclei are passing through
V : flow velocity

In the case of propeller tip vortex cavitation on a model scale propeller, the flow speed in the tip vortex is of magnitude 20m/s and cross section is about 1mm^2. An event rate of 1 cavitating nucleus per second leads to nuclei concentration of 0.05 nuclei / cm^3 (50 nuclei/liter). This gives an idea of the range of concentration we have to look at.

We present hereafter a comparison of three techniques that have been developed to measure the nuclei content in the GTH.

CENTER BODY SUSCEPTIBILITY METER TECHNIQUE

YLec Consultants along with CERG-Fluides has developed for DGA Techniques hydrodynamiques a reference technique for measuring the nuclei content [Pham & al, 1993]. This technique is called Centrebody Susceptibility Meter (CSM) (or also called Venturix in this last version) which measures directly the critical pressure of cavitation nuclei. The technique is based on the principle of a Venturi. At the nozzle throat of the Venturi, the pressure is a function of the flow rate and the upstream pressure. The minimum pressure at the nozzle throat can reach values lower than the vapour pressure and even a negative pressure.
The CSM Venturix has been designed to eliminate some drawbacks of former designs and permit a very precise measurement of the throat pressure.

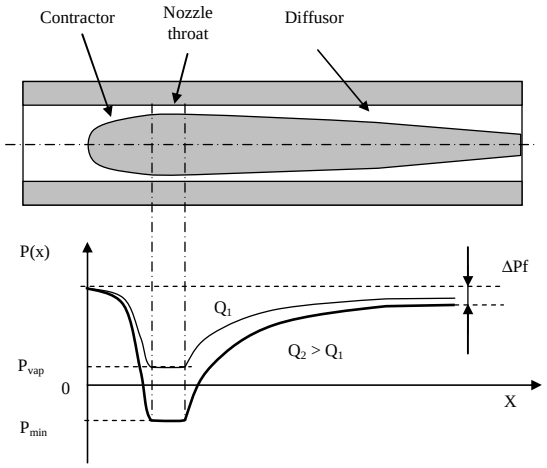

Figure 1: CSM principle

The theoretical relationship (quasi-static theory) between the nuclei size and critical pressure is given by the Rayleigh Plesset equation [Rayleigh, 1917, Plesset 1949]:

$$p_{crit} = p_{vap} - \frac{4S}{3R_{crit}} \quad \text{eq(1)}$$

$$R_{crit} = \sqrt{\frac{3\left(P_0 - p_{vap} + \frac{2S}{R_0}\right)R_0^3}{2S}} \quad \text{eq(2)}$$

P_{crit} : nucleus critical pressure
p_{vap} : vapour pressure at a given temperature
P_0 : local pressure
R_0 : nucleus initial radius
S : surface tension between air and water

The nuclei content can be measured by a Centerbody Susceptibility Meter (CSM) in the cavitation tunnel. The device is composed of a sampling probe installed in the tunnel, either in the test section for special calibration purposes, or at the inlet of the contraction for routine tests. A flow rate of about 1 liter/s passes through the Venturi and then comes back to the tunnel. For a high enough flow rate the minimum pressure p_t at the venturi throat will enable all the nuclei whose critical pressure is higher than p_t to produce vapour bubbles. The number of these active nuclei per time unit is measured by an acoustic counting of the bubbles collapses. A piezo-ceramic cell and a dedicated signal processor are used for this purpose. Using the flow rate passing through the Venturi, the counted number per second is then transformed into concentration. A cumulative distribution of the nuclei critical pressure is then derived from measurement done at different sampling flow rate.

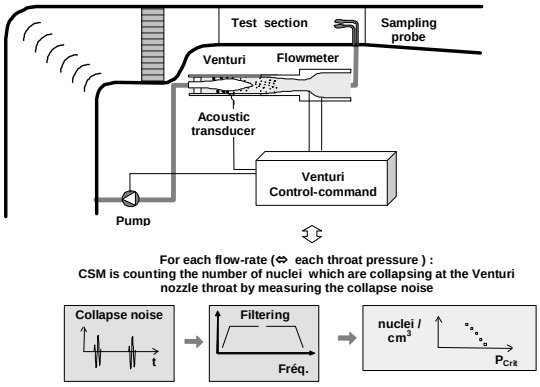

Figure 2: CSM set up in the test section

The nozzle throat pressure is calculated from measurements of the flow rate (differential pressure in a contraction) and of the absolute pressure upstream from the Venturi, using a Bernoulli equation in which the Reynolds effect on the effective section at the nozzle throat is integrated through a pressure coefficient Cp_{min}.

$$P_{THROAT} = P_{UPSTREAM} + Cp_{\min} \cdot \frac{1}{2} \cdot \rho \cdot \left(\frac{Q_V}{S_{THROAT}} \right)^2 \quad \text{eq(3)}$$

P_{THROAT} : static pressure at the nozzle throat
$P_{UPSTREAM}$: static pressure upstream from the nozzle throat
Cp_{min} : pressure coefficient at the nozzle throat
Q_V : flow rate through the nozzle
S_{THROAT} : cross section area at the nozzle throat

A calibration of the Reynolds effect on the Cp_{min} has been done and compared through CFD calculation on the boundary layer development [Pham & al, 1993].

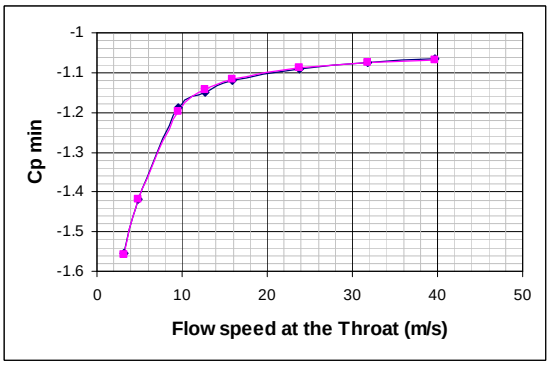

Figure 3: Reynolds effect calibration of the Venturi

This method provides directly the right information for cavitation tests which is the density of active nuclei at each pressure level. It must be emphasized that Venturi can be used to measure the critical pressures not only of artificial microbubbles as those injected in the GTH, but also the critical pressures of nuclei in natural waters or in other fluids like liquid metals. They can measure very low susceptibilities down to -5 to -10 bar for example.

From eq(1) & eq(2), we can calculate the relation between nuclei critical pressure and nuclei sizes for a given flow pressure P_0.

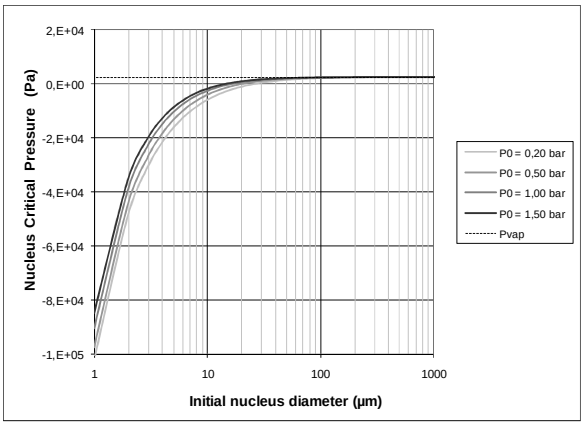

Figure 4: Nuclei critical pressure and Nuclei Diameter relation

From Figure 4, we can see that cavitation occurs at pressure levels close to the vapour pressure when the nuclei diameter is above 50µm. If we put it the other way, we can see that large sizes nuclei have the same critical pressure which is the vapour pressure (about 2500 Pa).
The transformation of the nuclei critical pressure into a nuclei diameter, also points out that the uncertainty on the nuclei diameter is very large for the largest nuclei sizes, because a small error on the critical pressure gives a large error on the nuclei diameter. This means that, when it is possible to know the nature of particles and measure their size, it will be easier to transform sizes distribution in critical pressure than doing the reverse transformation.

<u>Uncertainty analysis:</u>
For nuclei critical pressure close to the absolute zero pressure or close to the vapour pressure (2450 Pa), the accuracy of the throat pressure is very poor, for it comes from a subtraction of two terms which are very large.

$$P_{THROAT} << P_{UPSTREAM} \approx Cp_{\min} \cdot \frac{1}{2} \cdot \rho \cdot \left(\frac{Q_V}{S_{THROAT}} \right)^2 \quad \text{eq.(5)}$$

This remark emphasizes the needs of a very good accuracy on the actual section at the Venturi throat as well as on the upstream pressure and

the flow rate measurements, which is the case for the CSM Venturix.

Measurements done in the GTH in small test section :

Measurements have been done at one flow speed (6m/s) and 3 different flow pressures. The results are shown in the following figure.

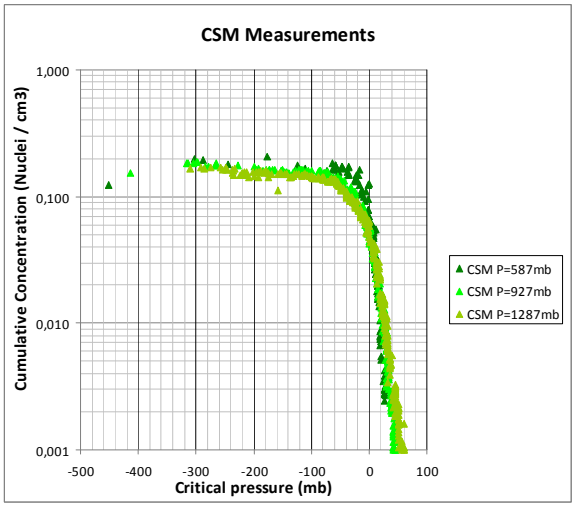

Figure 5: Critical pressure cumulative distribution

The preceding graph shows that most of the nuclei present in the flow have critical pressures close to the vapour pressure. The graph also shows that some nuclei seem to have critical pressures slightly above vapour pressure. This is due to the fact that the largest bubbles may become unstable and have a collapse which produces noise even under throat pressures slightly higher than their critical pressures. It is interesting to note that this phenomenon will also happen on the model.
Using the Rayleigh-Plesset equation, the nuclei distribution of critical pressure can be transformed into nuclei size distribution.

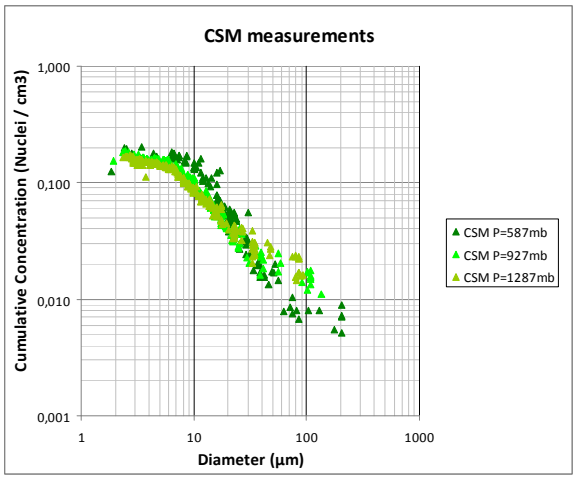

Figure 6 : Nuclei diameter cumulative distribution

Keeping in mind that large microbubbles, with a diameter larger than 50 µm have practically the same critical pressure, the CSM is able to give a rough idea of the nuclei size distribution. The smaller the nuclei are, the more accurate the evaluation of their equivalent diameter is.
Moreover, from the previous graphs, the range of diameters and concentrations to measure with the optical method has been identified as follows:

Nuclei size : 1 µm < D < 100 µm
Nuclei Concentration : 0.01/cm3 – 0.2/cm3

DIH TECHNIQUE

Principle of the Digital in line Holography technique:

The Digital In-line Holography (DIH) technique has been developed at CORIA (Université de Rouen) for droplets sizes measurements [Lebrun & al, 1999; Lebrun & al, 2003; Pu & al, 2005]. Its extension to micro-bubbles sizes measurements has been undertaken for nuclei measurement in the cavitation tunnel.
Digital In-line Holography (DIH) consists in reconstructing numerically an in-line hologram recorded by a 2D image sensor (CCD or CMOS camera). By adjusting the reconstruction distance (noted z) it is possible to rebuild, slice by slice, the interrogation volume that was illuminated by a Laser during the recording step.
In this application, the light, coming from a fibre-coupled Laser diode enables to illuminate the sample volume with a diverging beam. According to this configuration (also called Digital in-line Holographic microscopy), the numerical aperture can be increased and the reconstructed images

can be magnified. The magnification factor depends on the curvature radius of the recording wave. It must be pointed out that the light power required for DIH is very low because the forward scattering is used. In this experiment a 100 nJ Laser pulse is sufficient to record quite good holograms.
The following figures show the flow sampling hydraulic loop that is used for DIH measurements.

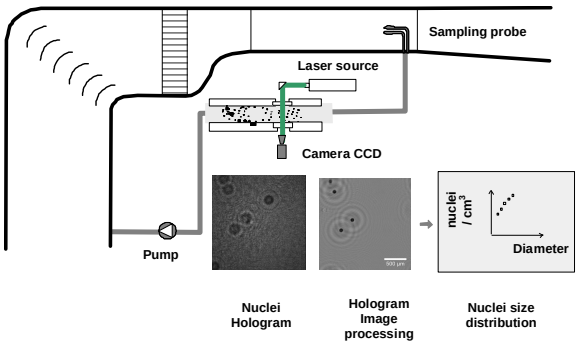

Figure 7: DIH setup in the GTH

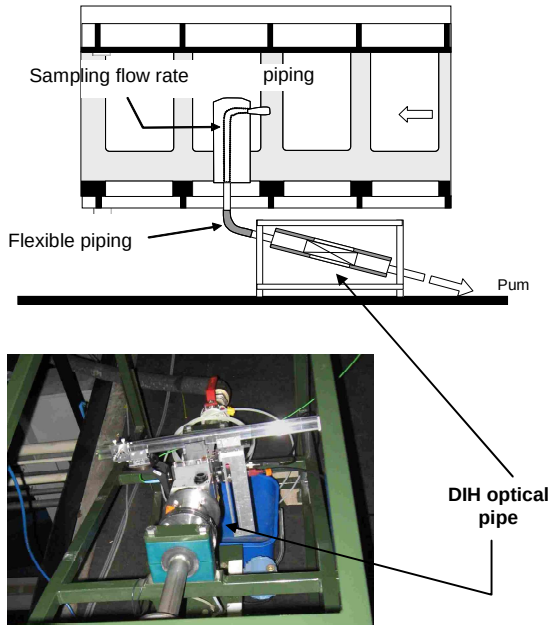

Figure 8: Experimental set-up in the cavitation tunnel

The same flow sampling hydraulic loop is used as for the CSM measurements. The only difference is that the Venturi part is replaced by a design dedicated optical part.

Note that a direct measurement in the test section (cross-section of 2m x 1,35m) with this equipment would have been difficult to perform for two reasons: at first, a specific optical system such as described in ref. [Malek et al. 2004] should have been designed to record particle holograms with an acceptable optical aperture. Secondly, a high power light source should have been required due to the absorption of the propagation medium (water).

Design of an optical pipe for the experimental set up in the GTH :

The flow sampling hydraulic loop includes an optical pipe which has an internal square section in order to have two planar optical windows. A cylindrical pipe, which would have been easier to manufacture, could have been used for these tests. However, the processing of digital holograms is not straightforward even if we have shown that the Fractional Fourier Transform must be used in this case to reconstruct images [Verrier & al, 2008]. Consequently, a pipe with a square cross section has been designed in order to simplify the computations and the interpretation of the results.

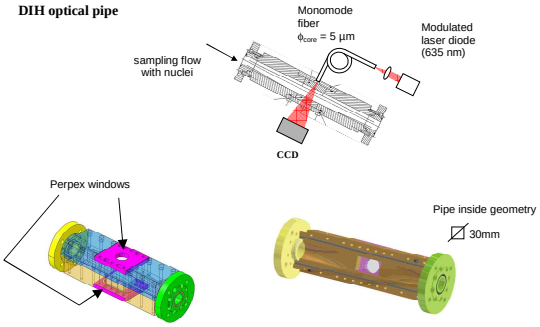

Figure 9: DIH optical pipe (details)

DIH image processing :

Let us describe the principle of the recording and reconstruction of digital holograms. Consider a particle located at a distance z_e from the recording plane. Under far-field approximation and assuming the object to be opaque, the intensity distribution recorded by the camera can be described by the following convolution:

$$I_{z_e}(x,y) = 1 - \left[O ** \left(h_{z_e} + \bar{h}_{z_e}\right)\right](x,y) \qquad \text{eq(6)}$$

where $1 - O(x,y)$ is the object transmission function (here a bubble) and

$$h_{z_e}(x,y) = \frac{1}{i\lambda z_e} exp\left[i\frac{\pi}{\lambda z_e}\left(x^2+y^2\right)\right]$$ the Fresnel Kernel.

As for the recording step, the intensity distribution in a reconstructed image located at a distance z_r from the camera is also calculated by a convolution operation:

$$R(x,y) = \left[I_{z_e} ** \left(h_{z_r} + \overline{h_{z_r}}\right)\right](x,y) \quad \text{eq(7)}$$

It is easy to show that when the best focus plane is reached (i.e. when $z_r=z_e=z$), we obtain :

$$R(x,y) = 2\left\{1 - O(x,y) - \frac{1}{2}\left[O(x,y) ** \left(h_{2z} + \overline{h_{2z}}\right)\right](x,y)\right\} \quad \text{eq(8)}$$

As shown by eq (8), the reconstructed image $1-O(x,y)$ is surrounded by the unwanted fringes pattern $\frac{1}{2}O(x,y) ** \left(h_{2z} + \overline{h_{2z}}\right)(x,y)$ also called « twin image ».

Fig.11 (a) illustrates an example of simulated hologram under plane wave configuration. The twin image effect (surrounding circular rings) can be observed on the profile of the reconstructed image (fig. 11 (b)).

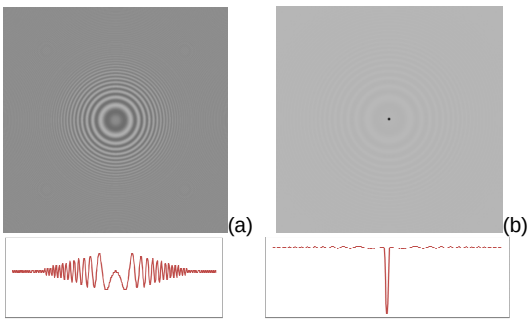

(a) (b)

Figure 10 : Hologram reconstruction : (a) hologram of a particle, (b) reconstructed image

It can be shown that the above reconstruction equation can be rewritten as a Wavelet Transformation (see reference [Buraga et al. 2000]). Thus, the best focus plane is founded by searching for the scale that leads to the maximum modulus of the wavelet transformation [Allano & al, 2005]. However, it should be noted that this criterion is limited to 3D localization of small particles (*d<20 µm* for the present configuration) . For larger nuclei, the Bexon criterion has been implemented [Bexon et al. 1976]. From a given reconstructed plane calculated at a distance z, a common particle-image sizing algorithm is used for nuclei diameter measurements. Typical image bubbles of both size ranges are presented on Fig. 11.

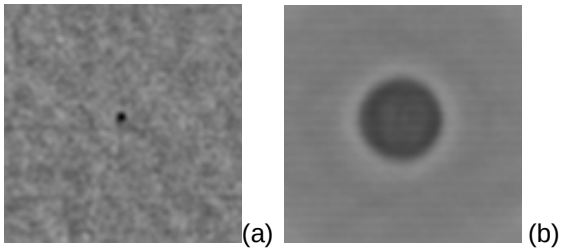

(a) (b)

Figure 11 : Examples of reconstructed particles holograms (a) small particle (d= 10 µm) and (b) large particle (d=85 µm)

Preliminary tests at CORIA :

Some preliminary tests were done using the optical part only. The optical probe is presented on *Figure* 12. The fiber-coupled Laser diode can be observed on the right-hand side of this figure. A CMOS 1280x1024 camera (left) records the diffraction patterns of bubbles introduced in the optical pipe.

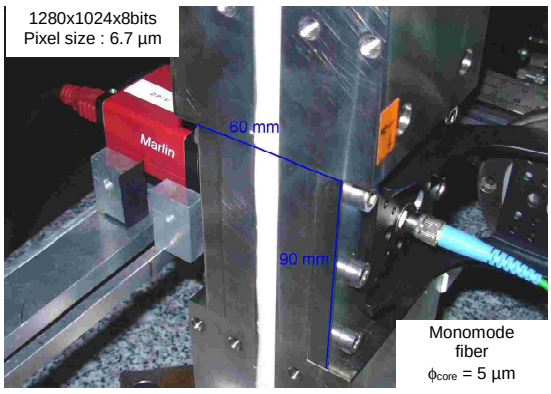

Figure 12: DIH setup at CORIA

The image (a) of *Figure* 13 gives an example of hologram recorded with this setup. Images (b), (c) and (d) illustrate respectively the images reconstructed at z=41.7mm, 49.2 mm and 55.1 mm in the optical pipe. A ratio between the grey levels of two successive recordings has been performed in order to increase the signal-to-noise ratio of holograms. This normalization enables to suppress the background variations due to the non-uniform illumination of the Laser beam. This is the reason why some bubble images appear in white (first exposure) and others in black (second exposure).

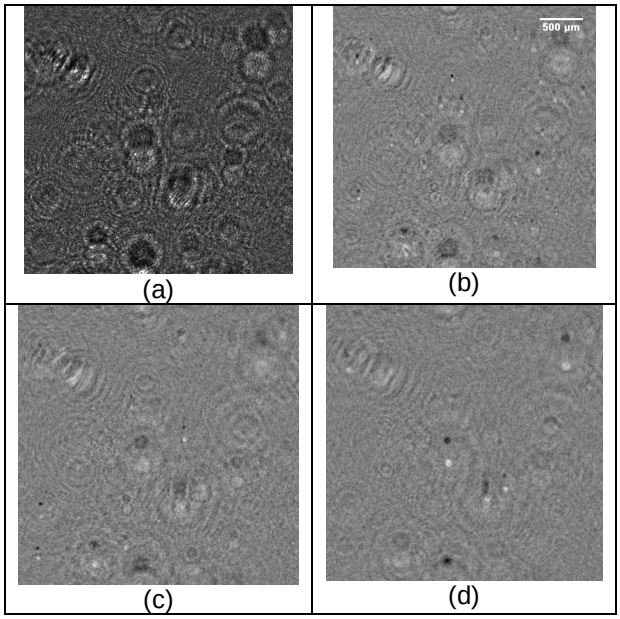

Figure 13: Digital holograms of bubbles.
(a) the hologram,
(b-d) reconstructed images at z=41.7mm, z=49.2 mm and z=55.1 mm

Nuclei measurement in the GTH with DIH :

The measurement campaign has been realized with the experimental setup described in previous section. More than 6000 holograms have been recorded with 3 different flow pressures. The following recording conditions are used:

Power from the fiber-coupled Laser diode	P = 0,15 mW
Distance from fiber-coupled Laser to flow sampling pipeCSM	11 mm
Distance flow sampling pipe CSM-camera	39 mm
Image size	1024 x 1024 pixels of 6.7 x 6.7 µm
Field of view :	few millimetres (depends on the magnification ratio)
Depth of field :	30 mm
Depth of the measuring volume	6 mm
Measuring volume	30 mm^3
Acquisition conditions	image Rate 5Hz ; time exposure 10 µs
Power from the fiber-coupled Laser diode	P = 0,15 mW

Table 1 : DIH optical set-up

Results are presented in *Figure* 14. 5841 particles have been detected in a sequence of 5000 holograms (total recording time of 1000 sec).

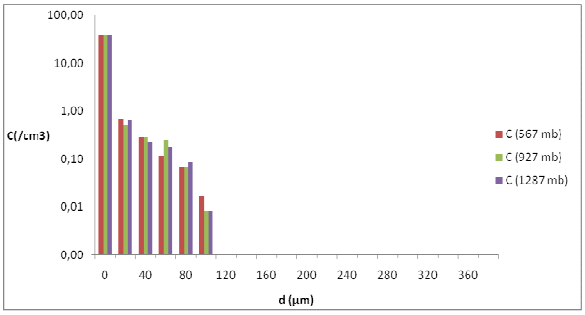

Figure 14: – Size nuclei distribution in the optical pipe for three different flow pressures (5881 particles detected).

At first, it must be noted that the minimum measured diameter with that configuration is about 7 µm. Secondly, the measured diameters of the smallest particles are probably overestimated because the low-pass filter introduced by the holographic system leads to a spreading of the reconstructed particle images.
This point will be taken into account in the future in order to improve the reliability of the measured size distributions.

ILI Technique principle

The Interferometric Laser Imaging Technique has been largely developed for droplets measurements but not for bubbles sizing, mainly because there are more industrial applications with droplets than with micro-bubbles.
The technique is using a Laser sheet that illuminates the particles in the flow and a camera that records images of particles passing through the Laser sheet. This technique is derived from Interferometric Laser Imaging Droplet Sizing (ILIDS) [Ragucci & al 1990, Glover & al 1995, Pu S. 2005]. In case of droplets, the scattered light from the spherical particle is an interference of the reflected light and the refracted light (first order of refraction mainly) through the particle. In the out of focus plane (see Figure 15), the circular boundary of the particle out of focus image, of diameter a, contains the same number of fringes N than the aperture D. a and D are related by

$$a = D\frac{L-l}{L} = D\frac{l_x}{L} \qquad \text{eq. (9)}$$

If the fringes frequency in the out of focus plane is denoted by f, i.e.,

$$f = \frac{N}{a} \qquad \text{eq. (10)}$$

the fringes spacing is written as

$$\Delta\theta = \frac{\alpha}{N} = \frac{\alpha}{af} \qquad \text{eq. (11)}$$

Considering a CCD camera in the out of focus plane to record the images, the number of fringes can be directly evaluated from the size of the circular boundary and the fringes frequency expressed in pixel and pixel^{-1} respectively, by

$$N = a_p \, f_p \qquad \text{eq. (12)}$$

leading to

$$\Delta\theta = \frac{\alpha}{a_p f_p} \qquad \text{eq. (13)}$$

Generally, the diameter of the droplets or bubbles is roughly inversely proportional to the fringes spacing $\Delta\theta$. The diameter of the particle d_p is then written as

$$d_p = \kappa \cdot \frac{1}{\Delta\theta} = \frac{\kappa \cdot a_p \cdot f_p}{\alpha} \qquad \text{eq. (14)}$$

In case of droplet with refractive index m, without any wall and for a scattering angle θ between 20° and 70° the following equation is deduced from geometrical optic considerations.

$$d_p = \frac{2 a f \lambda}{\alpha}\left(\cos\left(\frac{\theta}{2}\right) + \frac{m \sin\left(\frac{\theta}{2}\right)}{\sqrt{m^2 - 2m\cos\left(\frac{\theta}{2}\right)+1}}\right)^{-1} \qquad \text{eq. (15)}$$

that is to say

$$\kappa = 2\lambda\left(\cos\left(\frac{\theta}{2}\right) + \frac{m \sin\left(\frac{\theta}{2}\right)}{\sqrt{m^2 - 2m\cos\left(\frac{\theta}{2}\right)+1}}\right)^{-1} \qquad \text{eq. (16)}$$

For different scattering angle θ, the coefficient κ must be calculated using an adequate model (Lorenz-Mie Theory for example).

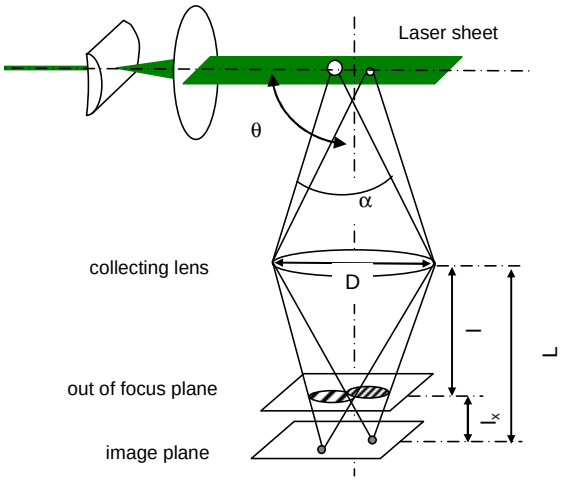

Figure 15: ILIT configuration

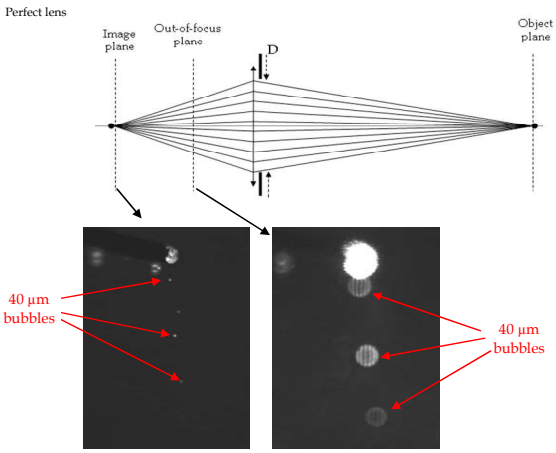

Figure 16: ILIT principle

In case of bubble, the refractive index changes from water to air. As illustrated in Figure 17, the collection angle in air and water, respectively, α and β are different. But the number of fringes contained in α is equal to the number of fringes contained in β.

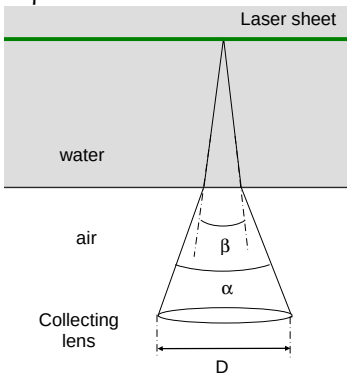

Figure 17: Optical path through water

So that the relation between bubble diameter and the number of recorded fringes becomes

$$d_{Bubble} = \frac{\kappa_w \ N}{\beta} = \kappa_w \ N \frac{n_{water}}{\alpha} \qquad \text{eq. (15)}$$

Where :

- $\kappa_w(n_{water}, \theta, \lambda)$ is a function of water refractive index n_{water}, scattering angle θ and wavelength λ. κ_w is calculated by using an optical scattering model (LMT). $\kappa_w \approx 52\,\mu m.\deg$ in our case.
- α is the collection angle in air, deduced from the calibration procedure.
- $N = a_p \ f_p$ is the number of fringes, with the circle radius a_p (in pixel) and the fringes frequency f_p (in Pixel^{-1}) deduced from image processing.

Specific requirements for nuclei measurements:

The lower limit of the ILIT for bubble size measurement is set by the lower number of fringes measurable in bubbles images. Let say that *N=2* fringes is a reasonable limit. From Eq. (15), it can be seen that a large collection α is needed to measure small bubbles. Considering the great distance at which the collection optics is set in our application (about 1 m), large lenses diameters are needed. The table 1 compares the minimum measurable diameter at 1 m distance (equivalent in air), with standard PIV system optics and with the first tested specific optical arrangement.

This first specific optical collection arrangement consists of a single spherical lens of large dimension (200 mm diameter). But due to spherical aberrations, the effective diameter of the optic was limited to 80 mm, for large out of focus positions. This effective diameter even reduces for smaller out of focus (with sensor closer to the image plane position). As a consequence, the theoretical lower limit, corresponding to an ideal 200 mm lens (d_{min}=12 µm) cannot be reached. Considering the effect of spherical aberrations, this limit is moved to 30 µm for the maximum out of focus position considered. Note that for this maximum out of focus position, the fiber image covers one half of the sensor. In case of bubble, measurements will be then limited to one bubble at a time.

Optical arrangement	Optics diameter / focal length / (aperture)	Minimum measurable diameters (for N=2 fringes)
Standard optical arrangement of PIV system	D=21.43 mm / f=60mm / (f/D=2.8)	d_{min}=112.5 µm
First optical arrangement (Large diameter Spherical lens)	D=200 mm (D_{eff}=80 mm) / f=450 mm / (f/D_{eff}=5.625)	d_{min}=30 µm
Ideal 200 mm lens	D=200 mm / f=450 mm / (f/D=2.25)	d_{min}=12 µm

Table 1: Optical characteristics

Spherical aberration is a well known limitation in classical imaging but it has never been studied in case of out of focus imaging (ILIT or ILIDS). The spherical aberrations responsible for the small size limitation in ILIT are illustrated in Figure 18, where out of focus images of a glass fiber are shown. Optical rays traveling near the lens center are focusing at a larger distance than optical rays traveling near the lens edges. As a consequence, fringes frequency is no more constant over the out of focus image. The fringes are closing at the image edges, even in case of largest out of focus (out of focus planes closer to the lens on Figure 19). For Smaller out of focus (closer to the image plane), external fringes are progressively lost and recover the central fringes. The effective lens aperture is then progressively reducing with decreasing out of focus distance.

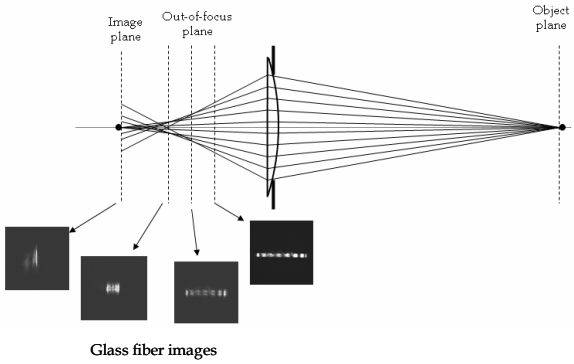

Figure 18 : Spherical aberration

A second specific optical collection arrangement has been designed to allow small nuclei size measurement. Specific lenses have been designed and manufactured to eliminate spherical aberration, and to keep a large aperture optical system (see Figure 19). The optical arrangement consists of two plano-convex lenses in order to reduce the other geometrical aberrations, responsible for distortions of images at the edges

of the sensor. One of these lenses has an aspherical profile in order to eliminate spherical aberrations.

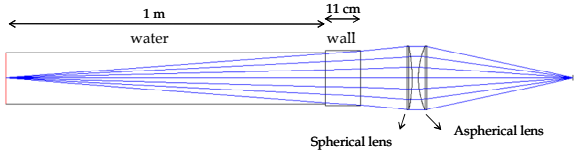

Figure 19 : Two lenses optical arrangement

The effective aperture of the optics has been experimentally checked to be 190 mm, as expected. The corresponding minimum bubble diameter (for two fringes) is 12.68 µm. The effect on manufacturing default on the lenses surfaces have been observed on the out of focus images. Circular structures are clearly visible but the linear fringes frequency measurement is not strongly affected (see Figure 20).
Note that chromatic aberrations are not considered because the Laser illumination is monochromatic.

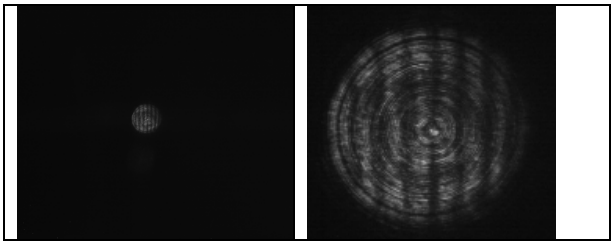

Figure 20: Out of focus images recorded with the specific optical arrangement.

ILIT Optical arrangement for GTH

Optical configuration :
The final optical arrangement designed for the GTH is summarized in the following table.

Laser sheet	perpendicular to tunnel walls
Angle between camera axis and Laser sheet :	$\theta = 90°$
lenses diameter	200 mm
Lenses effective aperture	190 mm
focal lens (in air)	325 mm
Object distance (equivalent in air)	1 m (= 644 mm in water +110 in plexi-glass+ 440mm in air)
Effective collection angle	10.85°
Field of view :	25mm × 19mm
Minimum bubble diameter (N=2) :	d_{min}=12.75 µm

Table 2 : Optical set up main characteristics

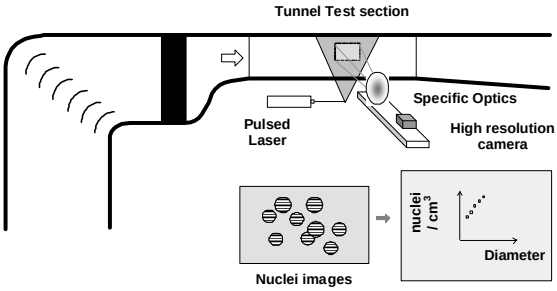

Figure 21: ILIT optical arrangement in cavitation tunnel.

Figure 22 shows a 58 µm bubble and a 12 µm bubble recorded with our specific optic.

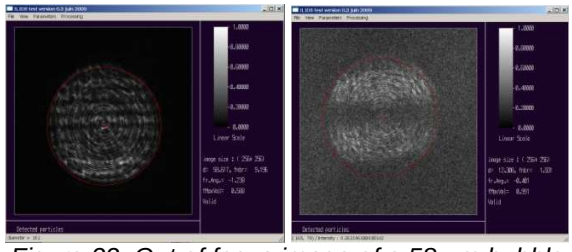

Figure 22: Out of focus image of a 58 µm bubble (left) and a 12 µm bubble (right) recorded by specific designed optics.

The lower limit reach by the technique fits our initial goal. This limit is fixed by the number of fringes (N≈1-2, depending on the image processing) and by the low contrast of the bubble image. The upper limit is fixed by the maximum measurable fringes frequency (depending on the pixel number and the out of focus position) but also by the intensity saturation of the CCD sensor. In fact, bubbles which are greater than 200 µm completely saturate the sensor. Fringes are no more visible and there is a significant risk of sensor deterioration.

Out of focus images have been simultaneously recorded on a second camera located at the same distance and equipped with a standard 60 mm objective (Table 3).

	Standard optic (1)	Specific Optic (2)
Focal lens (mm)	60	325.34
Lens Aperture (mm)	21.43 (f/D=2.8)	190
Optical distance Camera/Laser sheet (in air)	1000	1000
CCD size (pixel number) (7.4 µm^2)	1600 x 1200	1600 x 1200
Collection Angle α	1.23°	10.85°
Minimum diameter d_{min} (µm)	112.45	12.75
Magnification ratio	0.062	0.474

Table 3: standard & specific optical set-up

Results obtained with the two cameras are completely different. Camera 1 (standard optics) offers a larger field of view (192 x 144 mm) but only bubbles diameters bigger than 100 µm are measurable. Camera 2 offers a smaller field of view but bubbles diameters of the order of 10 µm are measurable. Figure 23 compares images of the same bubble recorded simultaneously with the two optical setups. With optics 1, the bubble image contains only about 3 fringes. With optics 2, it contains 28 fringes and the sensor is nearly saturated. The figure illustrates that the upper limit with optics 2 corresponds to the lower limit with optics 1.

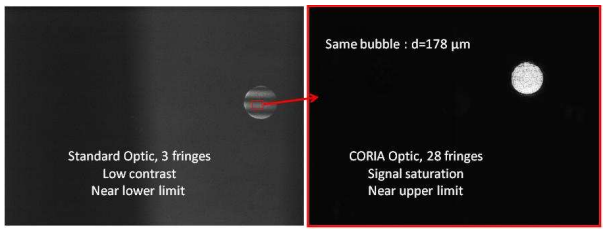

Figure 23: The same bubble simultaneously recorded with a standard optic (right) and the specifically design optics (left).

Calibration

The only needed calibration consists in evaluating the collection angle α. The following procedure can be applied to determine this angle α. The distance between the lenses and the camera is adjusted to focus on the Laser sheet in the tunnel. Then the assembly (lens + camera) is moved backward to image a target illuminated at the Laser light wavelength (532 nm), and the distance lens-target is measured. Knowing the effective diameter of the lens, α can be evaluated.

Conversely, one can set precisely to L=1 m (the distance for which the optics has been designed) the distance between the first lens and the target (in air). The focusing is next adjusted by moving the camera with respect to the lens. Then the whole optics (lens and camera) is moved forward to focus on the laser sheet. By doing so, the resulting collection, deduced from the lens effective aperture and the distance L is α=10.85°.

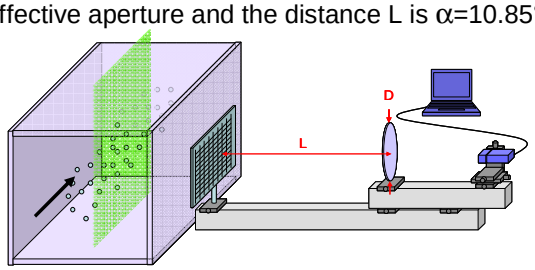

$$\alpha = 2\arctan\left(\frac{D_{effectif}}{2L}\right)$$

Figure 24: calibration procedure.

ILIT image processing

Although a first semi-automatic image processing has been implemented, the fully automatic image processing developed after is only presented. We should emphasize that all the steps of the automatic image processing have been optimized through the semi-automatic image processing.
The different steps of the image processing of the software are summarized in the following table:

1st step	Background subtraction and image enlargement.
2nd step	image filtering in the Fourier domain
3rd step	Particle images detection using a contour detection algorithm
4th step	Fringe number measurement and selection of bubbles among the detected particles

Table 4 : Image processing algorithm steps

Prior to image processing, a background image is subtracted to enhance the signal to noise ratio. The background image is built from a large number of images recorded in the same conditions. Next, an image processing area is defined: width and height of this area count a power of 2 of pixel (2^n where n is an integer) in order to allow the use of Fast Fourier Transform algorithms. To process 1600 x 1200 pixels images, they are first enlarged to 2048 x 2048 pixels. The grey level of the additional part of the image is set to the average grey level of the image boundary (see Figure 25).

The second step of the image processing consists in a high frequency filtering. This step makes

easier the following step (particle images detection) by removing or smoothing the fringes. Figure 26 shows the filtered image.

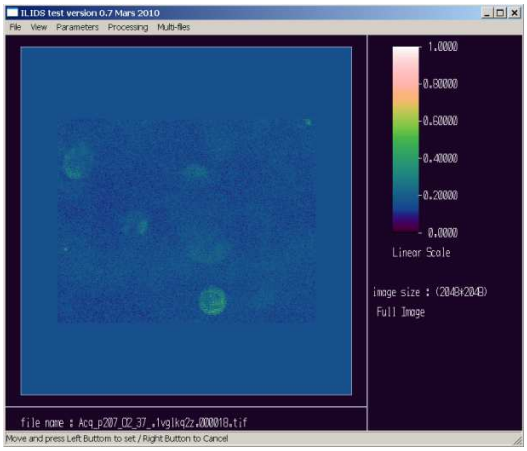

Figure 25 : enlarged image

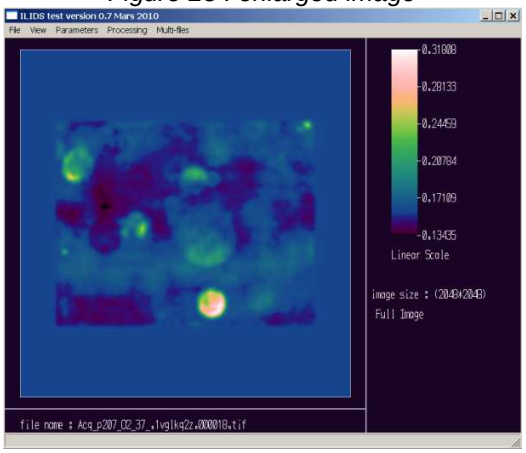

Figure 26: filtered image.

In the third step, the particle images detection (we do not know yet if particles are bubbles or not) begins by a contour detection. For the detection, a spatial derivative of the image is computed and its level is normalized (Figure 27). The resulting image is called the contour image.

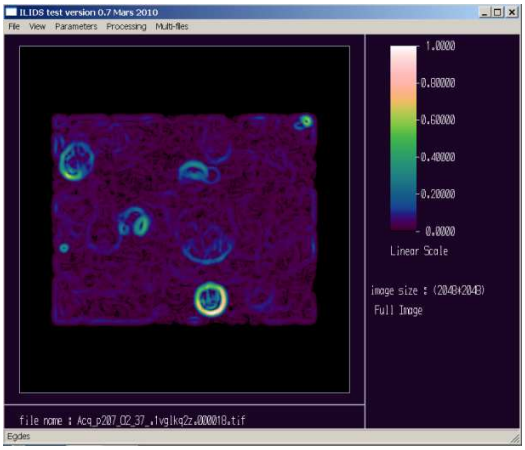

Figure 27: Contour Image.

The particles detection is completed using a convolution calculation between the contour image derivation and a reference image. The reference image consists of a ring with the same diameter than the particle image with a thickness of few pixels. Note that the particle image diameter does not depend on the bubble (or particle) diameter. It depends only on the out of focus level. In our case, the sensor has been moved forward by l_x=3 mm (see Figure 15). Knowing the lens diameter D, the distance between the lens and the sensor (l=450 mm) and the pixels size, the particle image diameter is found to be 170 pixels. This diameter can be also directly deduced from the images, leading to about the same value.

This step is completed by a local maximum detection in the convolution product result and a test based on particle image contrast. This technique allows overlapping particle image detection. When one (or several) particle is detected, the particle is removed from the contour image and replaced by a black disk. The contour image is then normalized again and a new convolution product is calculated. This iterative process allows the detection of several particles with high intensity contrast differences. In practice 3 or 4 iterations are enough to detect all the particle images. In the example of Figure 28, four particle images have been detected.

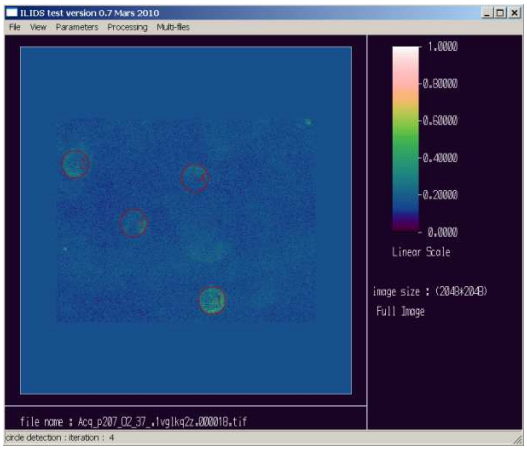

Figure 28 : Particle image detection

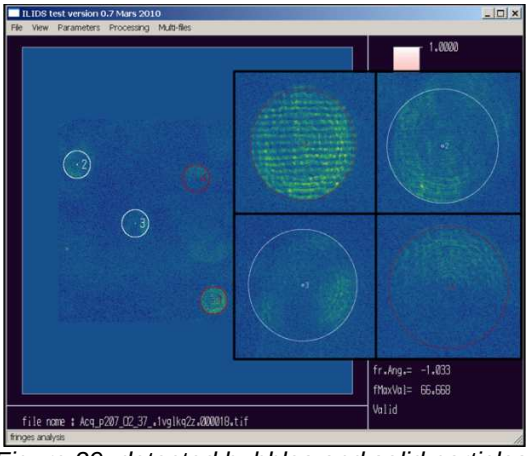

Figure 29: detected bubbles and solid particles.

The final step consists in measuring the fringes number for each detected particle. A 2D Fourier Transform is first computed. Fringes contrast and orientation are tested to separate bubble images from solid particle images. In case of overlapping particle images, the common areas are removed before the frequency analysis. The same precaution is taken for particle image partly cut on the image boundaries. In addition, the Fourier Transform of the particle image is compared to a reference disk Fourier Transform, before maximum frequency detection. This enhances the low frequency detection efficiency, associated to the small size bubbles. Figure 29 shows the detected bubbles (red circled) and the rejected images (solid particles circled in white). Finally, the bubble diameter is deduced from the measured fringes number and optical parameters, following Eq. (15). In Figure 29, Bubble 1 diameter is 104 µm, bubble 4 diameter is 9 µm, particle 2 and 3 have not been validated as bubbles. Note that the bubble 4 diameter is below the minimum diameter previously defined (12.75 µm), because the frequency analysis leads to a number of fringes lower than 2 (1.4). One could consider that such fringes number is not reliable and the corresponding bubble could be eliminated from the final result. However, such elimination can be achieved using a post-process.

Using our automatic image processing, about 18 hours are needed to process 1000 ILIT images on a laptop dual core CPU @2.3 GHz.

Evaluation of the image processing algorithm

The image processing algorithm was first applied to recorded images of one flow operating condition. Manual checking of each step of image processing has been done for this case. However, a visual validation of results is not obvious. Some bubble validation clearly appears erroneous but it is some time difficult to reject or to confirm bubble detection. So that, we sort the results in 3 categories: proper validation, erroneous validation and ambiguous cases. Figure 30 shows the distribution obtained with the automatic image processing (in blue) and the same distribution after 2 manual/visual selections. In selection 1 (in green), the wrong validation has been removed. In selection 2 (in red), both the wrong validations and ambiguous cases have been removed from the results. Differences (errors and potential errors) mainly relate the smallest bubbles diameter class and the error percentage is significant with respect to the bubble number. However, it must be noted that the solid particle concentration is about 20 times greater than the bubble concentration (see table 5 below). So that, with respect to total number of detected objects, the percentage of errors remains very low.

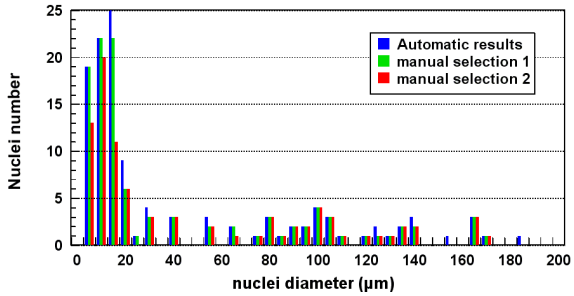

Figure 30 : automatic process evaluation.

Measurement volume and bubble concentration

The measurement volume is needed to deduce nuclei concentration from the measurement. The determination of the measurement volume for a 2D illumination based technique is always a

difficult task. However, this volume can be roughly evaluated from a Laser sheet profile measurements and from the field of view (CCD size and magnification ratio). The Laser sheet profile has been measured by displacing a scattering object (glass fiber) perpendicularly to the Laser sheet and a scattered intensity measurement. The profile width has been evaluated to be about 650 µm (at 1/e of the maximum intensity). The field of view is 25×19 mm^2. The measurement volume corresponding to one image is then estimated to about 0.3 cm^3. Then, a cumulative concentration distribution can be deduced from the distribution of Figure 30, as shown in Figure 31.

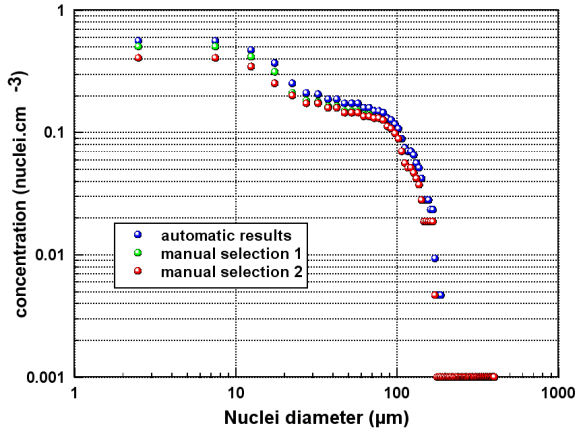

Figure 31 : cumulative concentration distribution.

Figure 31 shows the concentration of bubbles with a diameter greater than d as a function of d. The red curve (manual selection 2) can be viewed, as for Figure 30, as a minimum concentration. The green curve (manual selection 1) can be viewed as a credible result and remains close to the concentration distribution directly provided by the automatic processing algorithm (blue curve). At least, one can say that the difference between these two curves is weak compared to other source of uncertainty.

In particular, a constant measurement volume ($0.3cm^3$) has been assumed to deduce bubbles concentration from ILIT results. However, it must be noted that the actual measurement volume depends on the bubble size. The scattered light intensity is roughly proportional to square of the bubble diameter and the laser sheet intensity profile shows a gradual (and not sudden) decreasing. As a consequence the effective laser sheet thickness depends on the bubble size (larger for bigger bubble). If the measurement volume assumed here is a good estimation for the smallest bubble, it is clearly underestimated for the biggest ones. In the near future, better measurement volume estimation should be obtained by analyzing variations in particle image size, which depend on the out of focus level and then depends on the bubble distance from the optics. Such variations are clearly visible on the biggest bubble image but this has not been systematically measured by now.

Solid particles

In ILIT measurement, the image of any particle has a circular shape (corresponding to the circular shape of the collection optics). If the particle is spherical and transparent (bubble), the inside pattern of the circular shape is made of horizontal fringes. If the particle is opaque and of random shape, the inside pattern is no more regular, which is helpful to discriminate bubbles from solid particles. The image processing algorithm looks prior for circular shape before doing the 2D transform which is then used to identify if the particle is a bubble or not. The algorithm then provides the number of particles detected and the number of micro-bubbles. However, no information on the solid particle size is provided. On the three data collections corresponding to the three operating conditions, the total number of detected particles is almost constant and of about 2500 particles. Among those particles, about 140 are micro-bubbles (Table 5).

Flow operating condition (Test section pressure)	567 mbar	927 mbar	1287 mbar
Total number of particles / 1000 images	2543	2453	2545
Total number of bubbles / 1000 images	134	146	122
Ratio of bubbles number / particle number	5.3%	6.0%	4.8%

Table 5: Ratio of particle and bubbles detected

NUCLEI MEASUREMENTS DONE IN THE FRENCH LARGE CAVITATION TUNNEL (GTH)

To compare results obtained with the three different techniques, nuclei content has been measured in the small test section of the French large cavitation tunnel so called GTH. The operating conditions were as following:

- three different pressure conditions in tunnel have been considered (P=567mb , 927mb and 1287 mb),
- one flow speed (V=6m/s),
- the dissolved air content level was kept constant in between 30% and 34% of the saturation at atmospheric pressure,

- nuclei injection set with identical process parameters for all flow operating condition.

Each measurement corresponding to one technique was not done at the same time. DIH were done first, then CSM measurements and then ILIT measurements. Previous CSM measurements did show that if, the flow operating conditions are the same, the nuclei distribution is exactly the same because of the design of the cavitation tunnel.

A great number of images have been recorded for both ILIT and DIH measurements and size distribution has been converted to cumulative concentration distribution to allow comparison with CSM results. Such a comparison between the 3 techniques is proposed in Figure 32.

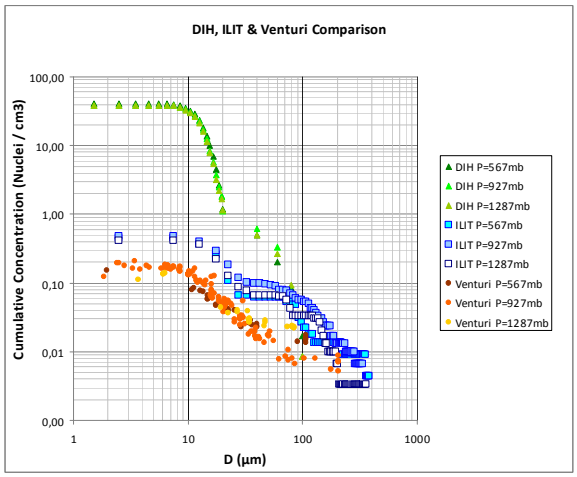

Figure 32 : *Nuclei cumulative concentration distribution obtained from DIH measurement, ILIT and CSM Venturix for three different pressure conditions in tunnel.*

The lower limit of the optical sizing techniques are similar (between 5 and 10 µm for DIH and about 10 µm for ILIT), so that the lower limit of size distribution are similar too. The major discrepancy between the optical technique DIH and ILIT is found for the small size nuclei. The concentration predicted by DIH is greater, because with the present DIH image processing, solid particles and bubbles are not distinguished. The solid particles are also visible in ILIT images for they can be identified by the absence of fringes. The solid particles concentration can be estimated from the ILIT processed images, to be about 20 times greater than the bubble concentration (see table 5). However, this estimation is very rough; ILIT processing is mainly focusing on bubble detection and many solid particles could be lost. The solid particle diameter cannot be evaluated from ILIT images but we expect that most of then are smaller than 20 µm, the size of the filters used in the tunnel. From Figure 32, the nuclei concentration measured with DIH is 80 times greater than the one measured with ILIT for the smallest sizes, under 10 µm. This ratio decreases down to about 20 for 20µm bubbles, and for bubble sizes greater than 80 µm concentration measured with both optical techniques are of the same order. In the future, a sphericity test could be included in DIH image processing in order to isolate solid particles from bubbles, at least for the greater sizes (Figure 33).

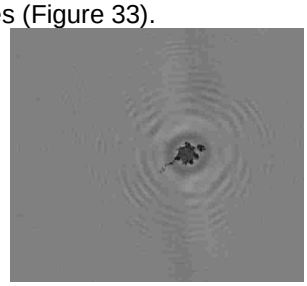

Figure 33: Hologram of a solid particle selected as spherical bubble of 123µm

Now, if we compare the results in terms of critical pressure, the nuclei distribution measured with DIH and ILIT differs somehow to the one measured with the CSM technique (See Figure 23). The maximum concentration found is 3 times higher with the ILIT. This discrepancy might come from the fact that the measuring volume should not be taken constant for the whole range of nuclei sizes. Large bubbles have a higher brightness even if they are in the edge of the Laser sheet. The variation of the measuring volume size is estimated to vary within a factor of 3 to 10.

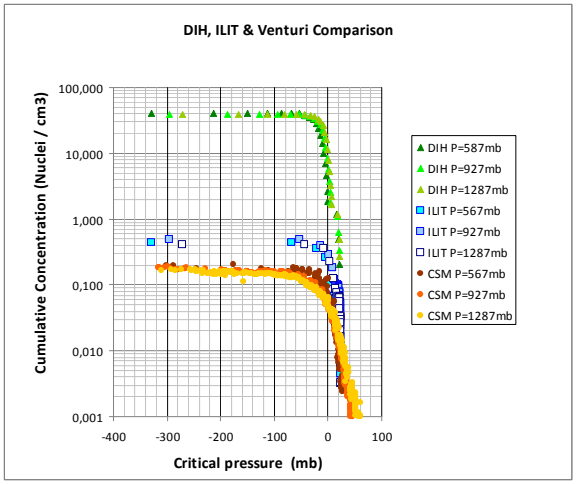

Figure 34: Comparison of cumulative distribution of nuclei critical pressure measured with different techniques for three different pressure conditions in tunnel.

CONCLUSIONS

Two new optical techniques have been successfully developed for nuclei measurement in cavitation tunnel. Those techniques have been then used along with a reference technique so called CSM or Venturix (Centerbody Susceptibility Meter).

Although measurement of very small bubbles down to 10µm in diameter was a real challenge in large cavitation tunnel, the Digital In Line Holography technique as well as the Interferometric Laser Imaging Techniques developed were able to measure a wide range of nuclei size diameter typically from 10µm up to 200µm. Both DIH and ILI techniques cannot give real time data for, the image processing is time consuming and the low nuclei concentration requires a large number of recorded images. The equipments needed for DIH is not very complex (a camera and a low power Laser source) but a sampling of the test section flow is compulsory. The equipments needed for the ILI techniques, although rather complex and expensive, is the same as for PIV systems except for the specific lens designed for small size measurements.
One critical point of DIH and ILI techniques is the definition of measurement volume which is needed to calculate the concentration.

The comparison of the nuclei size distributions measured by DIH and ILI techniques with the one of the CSM technique requires the transformation of nuclei critical pressure into nuclei diameter. Nevertheless the CSM provides directly the real information on the critical pressure of the water. The low level of concentration of the large nuclei does not make the optical measurements easy because a huge number of images is required to get a good statistical convergence of the concentration.

Besides those remarks, the main advantage of the optical techniques is to give a direct measurement of the nuclei size distribution which can be easily transformed in critical pressure.

Further investigations need to be done to address some of the issues of the two optical techniques used for cavitation nuclei measurements: measuring volume definition for ILI technique, possibility of solid particles and bubbles differentiation for DIH.

Acknowledgements :
This research work was partially supported by the EC project Hydro-Testing Alliance under the Joint Research Program JRP1 "PIV operation in hydrodynamic facilities". Hydro-Testing Alliance is the European Network of Excellence to facilitate the continuation of world leadership of the European Hydrodynamic testing facilities. HTA is supported by funding from the European Commission's Sixth Framework Programme under DG Research, project number 031316. The Network of Excellence started on the 1st of September 2006 and lasts five years.

BIBLIOGRAPHIC REFERENCES

Billet M.L., Wilson M.B., Bailo G.M., Gindroz B, Lee J.T, Bark G., Friesh J., Hoshino T, Szantyr J.A., "Report of the Cavitation Committee", Proceedings of the 21st ITTC, Tronheim, Norway,Vol. 1, 1996, pp. 63-126.

Gindroz B & Billet M.L., 1993, "Influence of the nuclei on the cavitation inception for different types of cavitation on ship propellers", ASME FED – Vol.177, New Orleans, USA.

Lecoffre Y., "Cavitation : bubble trackers" 1999, Ed. AA Balkema Publishers, Rotterdam Netherland.

Pham T, Michel J-M, Lecoffre Y., "A new design of the Cavitation Susceptibility Meter", Conference on cavitation, 1993, Birmingham, UK.

D'Agostino L. & Green S.I., "Simultaneous Cavitation Susceptibility Meter and Holographic Measurements of Nuclei in Liquids", Journal of Fluids Engineering Vol. 114, June 1992, pp261-267.

Buraga C., Coëtmellec C, Lebrun D. and Özkul C., "Application of wavelet transform to hologram analysis : three dimensional location of particles", Opt. and Lasers in Engineering, Vol 33 (6), 2000, pp 409-421

Pu C., Lebrun D., Allano D., Patte-Rouland B., Malek M., and Cen C.F.,"Particle field characterization by digital in-line holography: 3D location and sizing", Experiment in fluids 39, 2005, pp. 1-9.

Malek M, Lebrun D and Allano D, "Digital In-line holography system for 3D-3C Particle Tracking Velocimetry", A. Schröder, C.E. Willert (Eds.) : Particle Image Velocimetry, Topics Appl. Physics 112, ISBN : 978-3-540-73527-4, 2008, pp. 151-166

Verrier N., Coëtmellec S., Brunel M. and Lebrun D., "Digital in-line holography in thick optical systems: application to visualization in pipes", App. Opt. Vol. 47, 2008, n°. 22

Lebrun D, Benkouider A.M., Coëtmellec S., Malek M., "Particle field digital holography reconstruction in arbitrary titled planes", Opt Exp 11, 2003, pp. 3730-3734.

Lebrun D, Belaïd S., Özkul C., "Hologram reconstruction by use of optical wavelet transform", Applied Opt 38, 1999, pp. 3730-3734.

D. Allano, D. Lebrun, C. Buraga-Lefebvre, M. Malek, S. Coëtmellec, "Procédé de reconstruction d'hologrammes numériques par ondelettes", IDDN.FR.001.190024.000.S.P.2005.000.00000, Agence pour la protection des programmes, CNRS (2005)

Fréchou D., Dugué C., Briançon-Marjollet L., Fournier P., Darquier M. , Descotte L., Merle L., "Marine Propulsor noise investigation in the hydroacoustic water tunnel GTH ", 23rd Symposium on Naval Hydrodynamics, September 2000, France.

Glover A.R., Skippon S.M. and Boyle R.D.. "Interferometric Laser imaging for droplet sizing: a method for droplet-size measurement in sparse spray systems", Appl. Opt. 34 , 1995, pp. 8409-8421.

Oldenziel DM, Jansen R.H., Keller A.P. & Lecoffre Y. & Van Renesse R.L., "Comparison of Instruments for detection of Particles and bubbles in Water duringcavitation studies", Proceedings of IAHR Symposium on Operating Problems of Pump stations and Power Plants, Amsterdam, 1982.

Ragucci R., Cavaliere A., Massoli P., "Drop sizing by Laser light Scaterring Exploiting Intensity Angular oscillation in Mie Regime", Part. Syst. Charact. 7, 1990, pp. 221-225.

Pu S., "Development of interferometric methods for particle fields characterisation", Phd thesis, October 2005, Université de Rouen, France.

Rayleigh, "On the pressure developed in a liquid during the collapse of a spherical cavity", Phil. Mag, Vol 34, 1917, pp. 94-98.

Plesset M;S., "The dynamics of cavitation bubbles", Trans. ASME, Journal of Applied Mechanics, Vol 16., 1949, pp. 228-231.

Lecoffre Y, Chantrel P. & Tellier J., "Le Grand Tunnel Hydrodynamique (GTH)", ASME Winter Annual Meeting, Boston, USA, December 1987.

Bexon R, Gibbs J and Bishop GD, "Automatic assessment of aerosol holograms", Journal of aerosol science, Vol. 7, 1976, pp.397-407